

<https://doi.org/10.1038/s42005-025-02273-0>

Highly efficient broadband THz mixing and upconversion with Dirac materials

Check for updates

Tatiana A. Uaman Svetikova^{1,2}✉, Igor Ilyakov¹, Alexey Ponomaryov¹, Thales V. A. G. de Oliveira¹, Christian Berger³, Lena Fürst³, Florian Bayer³, Jan-Christoph Deinert¹, Gulloo Lal Prajapati¹, Atiq Arshad¹, Elena G. Novik², Alexej Pashkin¹, Manfred Helm^{1,2}, Stephan Winnerl¹, Hartmut Buhmann³, Laurens W. Molenkamp³, Tobias Kiessling³, Sergey Kovalev^{1,4} & Georgy V. Astakhov¹✉

The use of the THz frequency domain in future network generations offers an unparalleled level of capacity, which can enhance innovative applications in wireless communication, analytics, and imaging. Communication technologies rely on frequency mixing, enabling signals to be converted from one frequency to another and transmitted from a sender to a receiver. Technically, this process is implemented using nonlinear components such as diodes or transistors. However, the highest operating frequency of this approach is limited to sub-THz bands. Here, we demonstrate the upconversion of a weak sub-THz signal from a photoconductive antenna to multiple THz bands. The key element is a high-mobility HgTe-based heterostructure with electronic band inversion, leading to one of the strongest third-order nonlinearities among all materials in the THz range. Due to the Dirac character of electron dispersion, the highly intense sub-THz radiation is efficiently mixed with the antenna signal, resulting in a THz response at linear combinations of their frequencies. The field conversion efficiency above 2% is provided by a bare tensile-strained HgTe layer with a thickness below 100 nm at room temperature under ambient conditions. Devices based on Dirac materials allow for high degree of integration, with field-enhancing metamaterial structures, making them very promising for THz communication with unprecedented data transfer rate.

Frequency conversion is a key nonlinear phenomenon for wireless communication technologies when a weak low-frequency signal is mixed with a strong high-frequency carrier wave and transmitted from sender to receiver^{1–3}. The high carrier frequency allows for greater bandwidth, enabling faster data transfer and improved network performance. Due to the rapidly increasing demand for communication channels with ever higher speed and capacity, it is inevitable that the current microwave and mm-wave bands will be complemented with higher frequency bands located in the sub-terahertz (0.1–0.3 THz) and terahertz (0.3–3 THz) frequency domains^{4–6}. There are various approaches for frequency mixing in the mm-wave and sub-THz spectral regions based on different types of high electron mobility transistors^{7–9}. However, the practical implementation of on-chip frequency conversion in the THz domain still faces enormous and largely unexplored challenges.

Alternatively, frequency conversion can be achieved through four-wave mixing (FWM), which is caused by the third-order susceptibility $\chi^{(3)}$. A similar process is utilized for optical wavelength conversion in fiber-based telecommunication¹⁰. The conversion efficiency is proportional to $\chi^{(3)}d$, where d is the nonlinear medium thickness or the optical fiber length. FWM is also an essential tool for 2D spectroscopy in the THz domain, particularly, in narrow bandgap semiconductors^{11,12}, polar liquids¹³, molecular crystals¹⁴ and low-dimensional heterostructures¹⁵. Due to moderate $\chi^{(3)}$ and/or small d in these experiments, the frequency conversion efficiency is either comparably low or not specified. Highly efficient THz FWM has been reported for doped silicon¹⁶, provided by moderate $\chi^{(3)}$ and large $d = 275 \mu\text{m}$ ^{17,18}. The FWM measurements have been performed for bulk material at cryogenic temperature with the same incident frequencies, i.e., degenerate FWM, resulting in the third harmonic generation (THG). In contrast, for Dirac materials such as graphene¹⁹ and topological insulators^{16,20,21}, record-high

¹Helmholtz-Zentrum Dresden-Rossendorf, Dresden, Germany. ²Technische Universität Dresden, Dresden, Germany. ³Physikalisches Institut (EP3 and Institute for Topological Insulators), Universität Würzburg, Würzburg, Germany. ⁴Fakultät Physik, Technische Universität Dortmund, Dortmund, Germany.

✉e-mail: t.uaman-svetikova@hzdr.de; g.astakhov@hzdr.de

third-order nonlinearities have been observed, thus providing a promising material platform to exploit FWM processes further.

Here, we report a highly efficient conversion of the sub-THz broadband signal $f_a = 0.1\text{--}0.5$ THz from a photoconductive antenna (PCA)²² to the two THz bands $f_{\text{low}} = 0.9\text{--}1.3$ THz and $f_{\text{high}} = 1.5\text{--}1.9$ THz under ambient conditions. Our experimental setup is schematically presented in Fig. 1a. As a pump wave, we use narrow-band pulses from the superradiant accelerator-based source TELBE with a frequency around $f_T = 0.7$ THz²³. A Ti:sapphire amplifier synchronized with TELBE drives the PCA and also serves as a probe for the generated signals. FWM of the TELBE radiation and antenna signal results in $f_{\text{high,low}} = 2f_T \pm f_a$.

As a reference, we first measure the frequency dependence of the field conversion efficiency $\kappa(f_{\text{low}}) = E_{\text{low}}/E_a$ in monolayer graphene. It is less than 0.5%, as presented in the Supplementary Note 3. In the case of highly nonlinear HgTe-based heterostructures²¹, the upconversion efficiency is significantly higher and can reach $\kappa = 2.5\%$ (Supplementary Fig. S6). This observed enhancement does not follow a simple $\chi^{(3)}d$ scaling, as the overall efficiency depends on multiple factors including the carrier scattering time τ and the refractive index n_q . Usually, the performance of a frequency mixer is described in terms of the conversion loss $\text{CL} = -20\log_{10}\kappa$. It is presented in Fig. 1b for five PCA frequencies $f_{a,i}$ corresponding to the interference maxima in the sub-THz signal from the PCA (Supplementary Note 3). We note that this result is obtained in bare material with a thickness of only $d = 70$ nm.

Results

First, we measure the transmission of individual PCA and TELBE pulses through our HgTe layer separately, i.e., without their overlap and at normal incidence (Fig. 2a). To visualize their time-domain dynamics, we use electro-optical sampling (EOS) as schematically depicted in Fig. 1a (details

are described in Supplementary Methods). We observe multiple re-appearance of the pulses in the time domain due to reflection within the sample (Fig. 2b). The fast Fourier transformation (FFT) of the TELBE pulse results in a narrow peak at $f_T = 0.7$ THz (Fig. 2c). Therefore, we use only the primary EOS signal (the gray area in Fig. 2a) without considering the reflections. This approach ensures that there are sufficient points on the FFT peak to accurately represent it. The relevant PCA spectrum incident on the HgTe layer requires consideration of the entire range in the time domain, including several reflections Fig. 2a. The FFT of the PCA signal results in a broad frequency band $E_a(f_a)$ ranging from 0.1 THz to 0.5 THz (Fig. 2c). There are several interference peaks in the spectral domain ($f_{a,i}$), and their positions are identified from simulation of the multiple reflections (Supplementary Note 3). Upon observing the interference pattern (Fig. 2c), we reconstruct the initial PCA spectrum (Supplementary Fig. S5).

We experimentally verify THG at $3f_T \approx 2.1$ THz using high-power TELBE pulses with the maximum field strength $E_T^{\text{max}} \approx 86$ kV cm⁻¹, when they pass through the HgTe sample (Supplementary Fig. S4). From these measurements, we obtain the third order nonlinearity $\chi^{(3)} \approx 6.4 \times 10^{-10}$ m² V⁻², which is comparable to the record value reported for HgTe quantum well structures²¹ and graphene¹⁹ at room temperature. Note that this value is underestimated, as the complex multilayer structure of the sample and internal multiple reflections are not accounted. No THG is detected for the PCA signal with lower field strength $E_a^{\text{max}} \approx 6$ kV cm⁻¹.

After verifying the strong THz nonlinearity, we mix the PCA signal and TELBE beam in the HgTe sample. We use a combination of highpass, bandpass and lowpass filters to suppress spectral contributions below 1 THz from the fundamental harmonics of PCA and TELBE as well as above 2 THz from the third harmonic of TELBE (Supplementary Methods). The resulting time-domain signal is presented in Fig. 2d. The FFT of this signal shows two THz bands f_{high} and f_{low} (shaded area in Fig. 2e). This is a direct

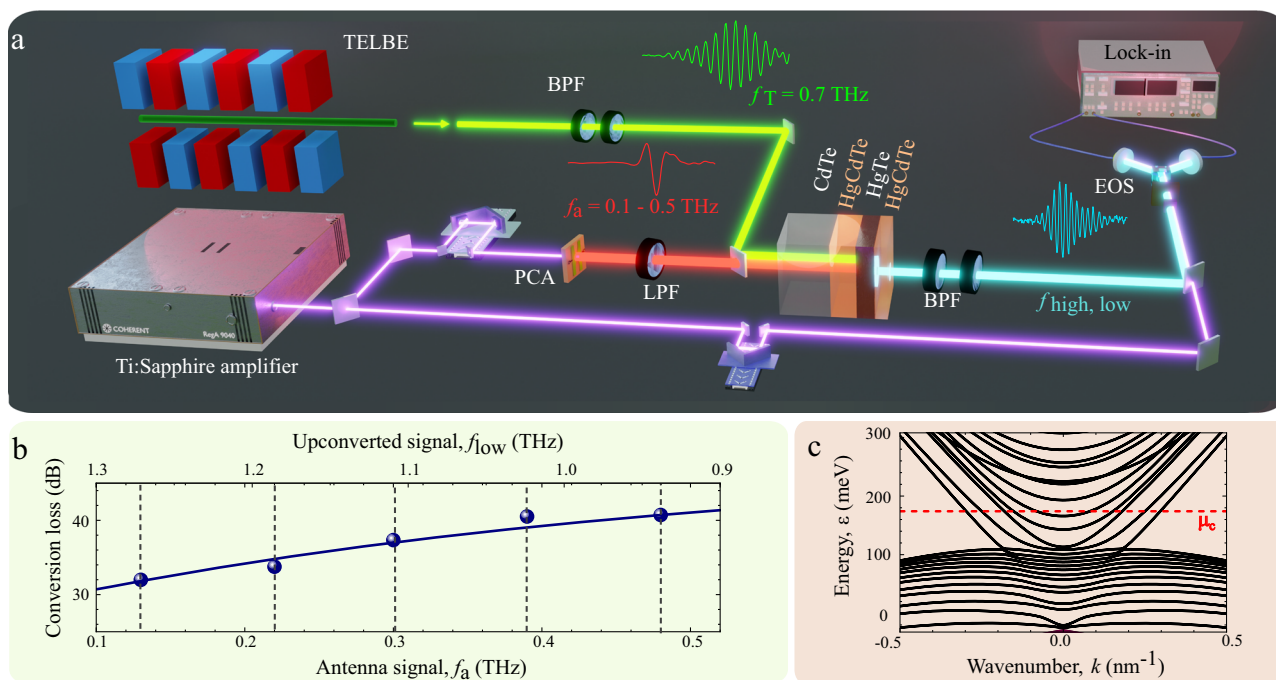


Fig. 1 | Upconversion of the broadband sub-THz signal at room temperature. **a** Schematic depiction of the experimental setup. High-power narrow-band THz pulses from TELBE with a frequency $f_T = 0.7$ THz are used as a pump wave. A Ti:sapphire amplifier is synchronized with TELBE and drives a photoconductive antenna (PCA). For the PCA, we used pulse energies of about $1 \mu\text{J}$ with a pulse duration of 35 fs. The broadband signal from the PCA $f_a = 0.1\text{--}0.5$ THz is upconverted to low and high THz bands using four-wave mixing (FWM) in a HgTe-based heterostructure and detected using electro-optical sampling (EOS). The setup includes band-pass filters (BPF) and low-pass filters (LPF) to select the desired spectral

components, as described in detail in the Supplementary Methods. **b** Conversion loss of the antenna signal $\text{CL} = -20\log_{10}\kappa(f_{a,i})$ in the low THz band $f_{\text{low}} = 2f_T - f_{a,i}$. Blue circles represent the experimental data. The vertical black dashed lines at frequencies $f_{a,i}$ indicate the interference maxima in the PCA signal. The blue solid line is a fit to an acceleration model. **c** The electronic band structure of the HgTe Dirac semimetal with a thickness of 70 nm is calculated using a $\mathbf{k} \cdot \mathbf{p}$ model for $T = 300$ K, as explained in the main text. The chemical potential μ_c , shown as red dashed line, is determined based on the carrier concentration and self-consistent calculation.

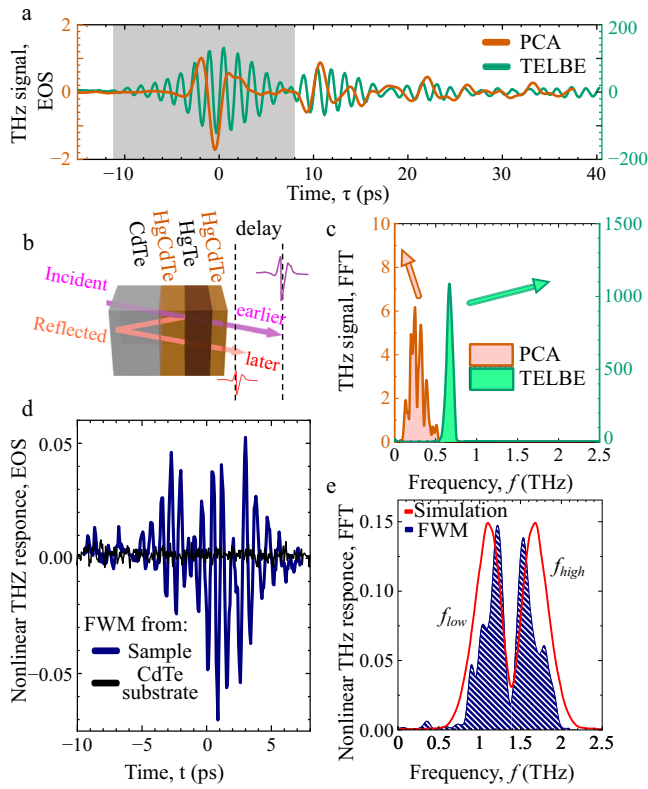


Fig. 2 | Terahertz four-wave mixing in a HgTe Dirac semimetal. **a** Time-domain dynamics of the sub-THz pulses from the TELBE facility (blue-green line) and a photoconductive antenna (PCA, red line) passed through the HgTe layer and detected with electro-optic sampling (EOS). The gray shaded area indicates the time window used to calculate the fast Fourier transform (FFT) spectrum from TELBE. **b** The echo is attributed to the internal reflection of the THz pulse, where the temporal signal shift directly corresponds to the sample thickness. **c** The power FFT of the time-domain sub-THz pulses from TELBE (blue-green) and PCA (red). **d** Time-domain dynamics of the resulting FWM signal. The black line shows a negligible FWM signal from the bare CdTe substrate. The THz fields from TELBE and PCA below 1 THz as well as the third harmonic from TELBE above 2 THz are suppressed in the detection path using bandpass filters (BPFs), as schematically shown in Fig. 1a. **e** The shaded area shows the power FFT of the THz FWM, revealing two pronounced maxima at the frequency sum $f_{\text{high}} = 2f_T + f_a$ and difference $f_{\text{low}} = 2f_T - f_a$. The red solid line shows the calculated spectrum as described in the text. The vertical axes in (a), (c), (d) and (e) are normalized such that the area under the power FFT from the PCA signal is equal 1.

manifestation of a highly efficient FWM process when the PCA frequency is subtracted from or added to the doubled TELBE frequency, $f_{\text{high}} = 2f_T + f_a$ or $f_{\text{low}} = 2f_T - f_a$, respectively. The field strength of the upconverted signal is given by (Supplementary Note 2)

$$E(f_{\text{high,low}}) \propto \chi^{(3)} d \cdot E_a(f_a) E_T^2(f_T) \cos(\alpha), \quad (1)$$

with α being the angle between the linear polarization planes of the TELBE and PCA waves.

Using Eq. (1) and the reconstructed spectra of the sub-THz fields from TELBE $E_T(f_T)$ and PCA $E_a(f_a)$ (Supplementary Note 3), we calculate the spectrum of the upconverted signal $E(f_{\text{high,low}})$. It is presented by the solid red line in Fig. 2e and shows a qualitatively good agreement with the experiment (the shaded area in Fig. 2e). The result of this fit is recalculated to the conversion loss, as presented by the solid line in Fig. 1b. The quantitative discrepancy with our experimental data may be related to the non-monotonic spectral characteristics of the bandpass filters. We also fit the spectral dependence of the conversion efficiency using asymptotic behavior

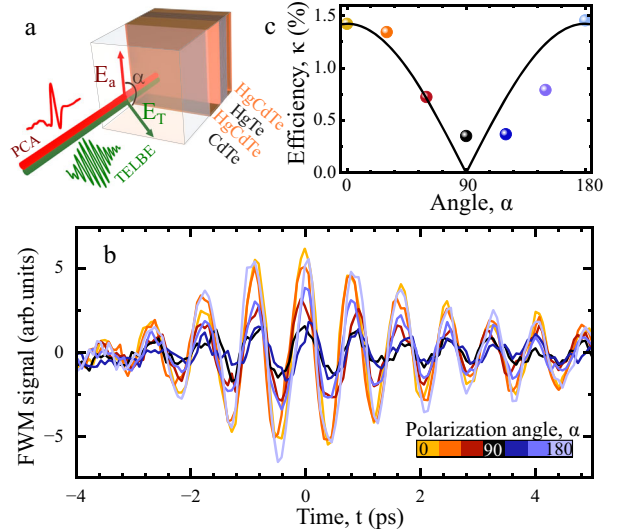


Fig. 3 | Polarization dependence of the terahertz four-wave mixing (FWM). **a** A scheme of the experiment showing the linear polarization of the TELBE (E_T) and the photoconductive antenna (PCA, E_a) THz fields. **b** Time-domain dynamics of the upconverted THz signal in the low THz band for different angles α between the polarization planes of the TELBE pump and PCA signal. Curves of different colors correspond to different angles α . **c** The THz upconversion efficiency for different α (symbols). The black solid line shows a fit proportional to $|\cos \alpha|$.

$\kappa(f_a) \propto 1/\sqrt{1 + (2\pi f_a \tau)^2}$ as shown in the Supplementary Fig. S3. The best fit is achieved with a scattering time $\tau \approx 0.5$ ps, which is longer than $\tau = 0.2$ ps obtained in our pump-probe experiments (Supplementary Note 1). Here, we do not consider the energy dependence of the scattering time $\tau(\mathcal{E})$, which is neglected in Eq. (2). In addition to that, many electron bands are occupied at room temperature (Fig. 1c), which have different contribution to the THz conversion due to different dispersion and possibly different scattering time.

To examine the applicability of the acceleration model for the description of FWM in HgTe Dirac semimetals with a long scattering time, we measure angular dependencies as schematically depicted in Fig. 3a. First, we verify that there is no statistically significant angular dependence in the third harmonic of the TELBE beam (Supplementary Methods). Then, we use a bandpass filter to selectively isolate the contribution from the low THz band. We fix the orientation of the linear polarization of the PCA signal and rotate the linear polarization plane of the TELBE wave. The maximum upconverted THz signal in the time domain is observed when the TELBE and PCA fields are parallel $\alpha = 0^\circ$ or 180° and minimum when they are perpendicular to each other $\alpha = 90^\circ$ (Fig. 3b).

We then measure the spectrally integrated conversion efficiency $\kappa = E_{\text{low}}/E_a$ as described in the Supplementary Note 3. The angular dependence $\kappa(\alpha)$ is presented in Fig. 3c. We observe a small but non-zero efficiency coefficient for the perpendicular polarizations of the PCA and TELBE fields. In the semiclassical approach of Eq. (1) (Supplementary Note 2), these coefficients are predicted to be zero. However, this model is oversimplified and neglects possible displacement in k -space during momentum scattering. More advanced theoretical models^{24,25} predict a non-zero efficiency coefficient for $\alpha = 90^\circ$, which aligns with our observations. On the other hand, the nonlinearity mechanism based on ultrafast heating and cooling^{26,27} is expected to have little to no angular dependence.

One of the most important characteristics of the frequency conversion is its dependence on the field strengths of the mixed waves, i.e., in our case from TELBE and PCA. The corresponding dependences of the time-domain signal in the low THz band are shown in Fig. 4a, b, respectively. Figure 4c shows the spectrally integrated wave-mixing field $E_{\text{low}}/E_{\text{low}}^{\text{max}}$ as a function of E_T . From a power-law fit to $(E_T)^\beta$, we obtain $\beta = 1.6 \pm 0.1$ (the dashed line in Fig. 4c). It is close to the expected value $\beta = 2$ from Eq. (1). A

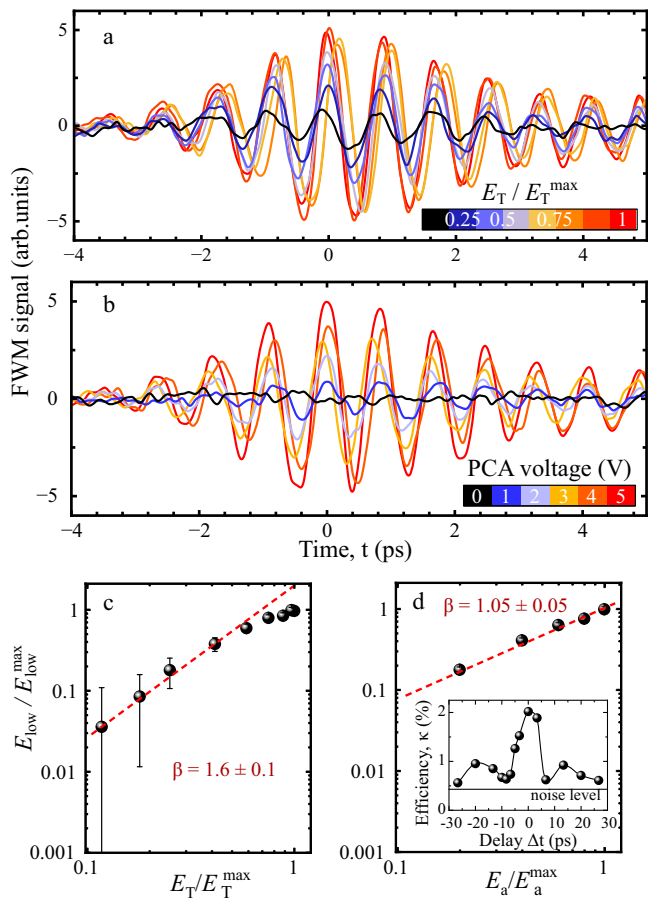


Fig. 4 | Field strength dependence of the four-wave mixing (FWM) in the low THz band for the parallel orientation of the TELBE and photoconductive antenna (PCA) fields. **a** Time-domain dynamics of the upconverted signal for different TELBE field strengths. The maximum field strength is $E_T^{\max} \approx 86 \text{ kV cm}^{-1}$. Curves of different colors correspond to different peak field strengths. **b** Time-domain dynamics of the upconverted signal in the low THz band for different voltages V_{PCA} applied to the PCA. The maximum field strength is $E_a^{\max} \approx 6 \text{ kV cm}^{-1}$ for $V_{\text{PCA}} = 5 \text{ V}$. Curves of different colors correspond to different V_{PCA} . **c** The FWM field $E_{\text{low}}/E_{\text{low}}^{\max}$ as a function of the normalized TELBE field strength for $E_a = E_a^{\max}$. The red dashed line is a fit to $\propto (E_T/E_T^{\max})^\beta$ of the five experimental points with lower E_T , yielding $\beta = 1.6 \pm 0.1$. **d** The FWM field $E_{\text{low}}/E_{\text{low}}^{\max}$ as a function of the normalized PCA field strength for $E_T = E_T^{\max}$. The red dashed line is a fit to $\propto (E_a/E_a^{\max})^\beta$ with $\beta = 1.05 \pm 0.05$. Inset shows the upconversion efficiency for different time delays between the TELBE and PCA pulses. The uncertainty of $E_{\text{low}}/E_{\text{low}}^{\max}$ was obtained by estimating the error of E_{low} from the noise floor and propagating it to the ratio using standard Gaussian error propagation. For some points error bars are smaller than the symbol size and thus not visible.

small discrepancy is related to the tendency to saturation for strong TELBE pulses, approaching the maximum value $E_T^{\max} \approx 86 \text{ kV cm}^{-1}$. We note that similar behavior is observed for THG (Supplementary Note 2). This saturation behavior can be attributed to a combination of carrier heating and nonlinear electron dynamics, consistent with both acceleration-based and thermodynamic (hot carrier) models of nonlinear transport in Dirac materials^{19,24,26,28,29}.

Figure 4 d presents the spectrally integrated FWM field $E_{\text{low}}/E_{\text{low}}^{\max}$ as a function of E_a . Similarly to the previous case, we fit it to a power-law fit to $(E_a)^\beta$ and we do observe linear dependence of E_{low} on E_a . This implies that $E_{\text{low}} = \kappa E_a$ with κ being independent of the PCA field strength in accord with Eq. (1). Finally, we examine the dependence of the conversion efficiency on the delay between the TELBE and PCA pulses. For delay times up to 2 ps, which is still shorter than the TELBE pulse duration but longer than the scattering time, we observe no significant dependence with $\kappa \approx 2\%$. The

time-resolved two-dimensional spectroscopy presented in the Supplementary Note 3 manifests the coherent dynamics of highly mobile Dirac carriers accelerated by sub-THz fields¹⁵.

With increasing time delay, there is a drastic decrease in the upconversion coefficient $\kappa = E_{\text{low}}/E_a$ (the inset of Fig. 4d). This decrease can be attributed to the diminishing overlap of the two beams as the time delay increases, resulting in reduced interaction between them. However, two secondary smaller peaks can be seen at positive and negative delays, which arise due to the signal/pump multiple reflections within the sample.

Discussion

In summary, we have upconverted a broadband sub-THz signal from a photoconductive antenna into THz bands using spectrally narrow intense pulses as a pump source. We achieve a field conversion efficiency of above 2% under ambient conditions at room temperature without any field-enhancing structures, corresponding to the intensity conversion loss less than 30 dB. Such an exceptional performance of a 70-nm-thick HgTe-based Dirac semimetal is ascribed to its very strong third-order susceptibility. According to our theoretical consideration, it is caused by a nearly linear dispersion of the surface Dirac states hybridized with bulk states and the long scattering time of electrons in these states. The last is especially important, as the third-order nonlinear response in the Drude regime scales strongly with τ .

Although the upconversion efficiency increases with the interaction length, it is fundamentally limited by absorption of the driving fields. Based on Drude-model estimates using our measured scattering time $\tau \approx 0.2 \text{ ps}$, the effective absorption coefficient at 0.7 THz is approximately $\alpha_{\text{eff}} \approx 540 \text{ cm}^{-1}$. This yields an optimal thickness of $d_{\text{opt}} \approx 8.5 \mu\text{m}$ for maximizing the FWM signal, assuming frequency-independent absorption as a first approximation (Supplementary Note 2). This estimate corresponds, in an idealized case, to converting nearly all incoming photons at the antenna frequency ($f_a = 0.25 \text{ THz}$) into photons at the upconverted frequency ($f_{\text{low}} \sim 1.15 \text{ THz}$). Because each upconverted photon carries more energy, the field upconversion efficiency may, in principle and without losses, exceed 100%. The coherence length for this process is approximately $4400 \mu\text{m}$, which is significantly larger than the thickness of our samples. Therefore, phase mismatch effects are negligible in our experiment, and coherence does not impose a practical limit on the upconversion efficiency.

Because the conversion efficiency scales with the thickness of the nonlinear medium, we expect its significant enhancement for superlattices based on HgTe/CdTe heterostructures, similar to multilayered graphene structures³⁰. Alternatively, the use of hybrid metamaterial structures^{31,32} and THz topological photonic structures integrated³³ with high-mobility Dirac materials could significantly improve the conversion efficiency and thus reduce the conversion losses by 20 dB, allowing for up- and downconversion of weak signals far above 100 GHz.

To contextualize the performance and integration potential of our $\chi^{(3)}$ -based four-wave mixing approach in strained HgTe, we perform a direct comparison with representative photo-assisted THz communication schemes, including electro-optic modulation (EOM)^{34–36}, photomixing^{37–39}, $\chi^{(2)}$ -based upconversion in inorganic and organic nonlinear crystals^{34,40} and difference frequency spectroscopy on surfaces of perovskite oxides⁴¹. As summarized in the Supplementary Note 4, our approach offers a significantly higher third-order nonlinearity, that operates without external bias or phase matching, and supports broadband, room-temperature functionality in an ultrathin geometry, making it attractive for future miniaturized THz systems.

While TELBE currently offers unmatched flexibility and field strength for nonlinear THz experiments, the use of compact sources such as quantum cascade lasers (QCLs)⁴² remains a promising avenue for future miniaturized or integrated nonlinear THz systems, especially when combined with local field enhancement strategies such as metasurfaces or THz resonators.

Summarizing, we envision integrable THz devices based on Dirac materials^{43,44} for on-chip signal modulation, mixing and, multiplexing in the THz frequency domain with unprecedented channel capacity, which may support data rates over 100 Gbps. With ultrawide bandwidths in the THz frequency domain, wireless connectivity will open up new possibilities for secure imaging, object positioning and intelligent interfaces.

Methods

The HgTe layer has a thickness $d = 70$ nm, which was determined using high-resolution x-ray diffraction (HRXRD) and x-ray reflectivity⁴⁵, and is grown by molecular beam epitaxy on a (001) CdTe substrate. The growth followed a substrate preparation with HCl to remove the native oxide. The HgTe layer is grown on top of a 110 nm Cd_{0.7}Hg_{0.3}Te buffer layer and capped by a 55 nm Cd_{0.7}Hg_{0.3}Te cap layer to protect it from surface oxidation⁴⁶. The buffer and cap layers have a bandgap of 800 meV. It is larger than TELBE and FELBE (free-electron laser facility) photon energies, ensuring that these layers are not excited in our experiments. Room temperature Hall characterization yields n-type carrier concentration of $3.4 \times 10^{12} \text{ cm}^{-2}$.

Due to the lattice mismatch between the CdTe substrate and the HgTe layer with the thickness $d = 70$ nm, a tensile strain opens a bandgap between the heavy- and light-hole bands in HgTe transforming it from bulk semimetal into a three-dimensional topological insulator with protected gapless surface states at low temperature⁴⁷, which becomes Dirac semimetal at room temperature. The energy dispersion $\mathcal{E}(k)$ is calculated using an eight-band $\mathbf{k} \cdot \mathbf{p}$ model within an envelope function approach⁴⁸, as presented in Fig. 1c⁴⁶. This model accounts for the strong coupling between the lowest conduction bands $|\Gamma_6, \pm \frac{1}{2}\rangle$ and the highest valence bands $|\Gamma_8, \pm \frac{1}{2}\rangle$, $|\Gamma_8, \pm \frac{3}{2}\rangle$, and $|\Gamma_7, \pm \frac{1}{2}\rangle$. It is based on an envelope-function approach introduced by Burt⁴⁹, with a proper operator ordering in the Hamiltonian, to definitively establish interface boundary conditions. The strain effects are taken into consideration by applying a formalism introduced by Bir and Pikus⁵⁰. Then, using the experimentally obtained carrier concentration, we determine the position of the chemical potential (Fig. 1c). It crosses the conduction bands with a nonparabolicity coefficient η approaching 1²¹, which is a necessary requirement for strong THz nonlinearity. This nonparabolicity is caused by the hybridization of the surface Dirac states and bulk states, which is further enhanced by the strong electrostatic repulsion stemming from the high carrier density at room temperature.

In the framework of the acceleration model^{21,24,28,51} and in the limit of $2\pi f_{\text{T}}\tau \ll 1$, the third-order nonlinearity is proportional to

$$\chi^{(3)} \propto \frac{\eta \tau^3 v_{\text{F}}}{k_{\text{F}}} \quad (2)$$

Here, k_{F} is the wavenumber and $v_{\text{F}} = \frac{1}{\hbar} \frac{d\mathcal{E}(k)}{dk}$ is the electron velocity averaged over all conduction-like bands in the vicinity of the chemical potential μ_{c} (Fig. 1c). According to Eq. (2), $\chi^{(3)}$ scales as the third power of the scattering time τ indicating that this parameter is crucial for strong THz nonlinearity. Therefore, we perform two-color pump-probe experiment at the FELBE facility to determine the scattering time τ of Dirac electrons in our system (Supplementary Note 1). From a Drude-type fit of the THz conductivity, we obtain the scattering time $\tau \approx 0.2$ ps, which is longer than in other Dirac materials^{19,20,52,53}.

Data availability

The data to reproduce figures from this study are available at RODARE, 2025, <https://doi.org/10.14278/rodare.3885>.

Received: 28 February 2025; Accepted: 12 August 2025;

Published online: 01 September 2025

References

- Kleine-Ostmann, T. & Nagatsuma, T. A review on terahertz communications research. *J. Infrared Millim. Terahertz Waves* **32**, 143–171 (2011).
- Wolff, P. A. & Pearson, G. A. Theory of optical mixing by mobile carriers in semiconductors. *Phys. Rev. Lett.* **17**, 1015–1017 (1966).
- Patel, C. K. N., Slusher, R. E. & Fleury, P. A. Optical nonlinearities due to mobile carriers in semiconductors. *Phys. Rev. Lett.* **17**, 1011–1014 (1966).
- Rappaport, T. S. et al. Wireless communications and applications above 100 GHz: opportunities and challenges for 6G and beyond. *IEEE Access* **7**, 78729–78757 (2019).
- Petrov, V., Bodet, D. & Singh, A. Mobile near-field terahertz communications for 6G and 7G networks: Research challenges. *Front. Commun. Netw.* **4**, 1151324 (2023).
- Salahdine, F., Han, T. & Zhang, N. 5G, 6G, and beyond: recent advances and future challenges. *Ann. Telecommun.* **78**, 525–549 (2023).
- Koenig, S. et al. Wireless sub-THz communication system with high data rate. *Nat. Photonics* **7**, 977–981 (2013).
- Hamada, H. et al. Millimeter-wave InP device technologies for ultra-high speed wireless communications toward beyond 5g. In *2019 IEEE International Electron Devices Meeting (IEDM)*, 9.2.1–9.2.4 (2019).
- Montanaro, A. et al. Optoelectronic mixing with high-frequency graphene transistors. *Nat. Commun.* **12**, 2728 (2021).
- Andrekson, P. A. Applications of nonlinear four-wave mixing in optical communication. *Optik* **279**, 170740 (2023).
- Junginger, F. et al. Nonperturbative interband response of a bulk insb semiconductor driven off resonantly by terahertz electromagnetic few-cycle pulses. *Phys. Rev. Lett.* **109**, 147403 (2012).
- Somma, C., Folpini, G., Reimann, K., Woerner, M. & Elsaesser, T. Two-phonon quantum coherences in indium antimonide studied by nonlinear two-dimensional terahertz spectroscopy. *Phys. Rev. Lett.* **116**, 177401 (2016).
- Runge, M., Reimann, K., Woerner, M. & Elsaesser, T. Nonlinear terahertz polarizability of electrons solvated in a polar liquid. *Phys. Rev. Lett.* **131**, 166902 (2023).
- Folpini, G. et al. Strong local-field enhancement of the nonlinear soft-mode response in a molecular crystal. *Phys. Rev. Lett.* **119**, 097404 (2017).
- Kuehn, W., Reimann, K., Woerner, M. & Elsaesser, T. Phase-resolved two-dimensional spectroscopy based on collinear n-wave mixing in the ultrafast time domain. *J. Chem. Phys.* **130**, 164503 (2009).
- Dessmann, N. et al. Highly efficient THz four-wave mixing in doped silicon. *Light Sci. Appl.* **10**, 71 (2021).
- Meng, F. et al. Intracavity third-harmonic generation in Si:B pumped by intense terahertz pulses. *Phys. Rev. B* **102**, 075205 (2020).
- Meng, F. et al. Higher-harmonic generation in boron-doped silicon from band carriers and bound-dopant photoionization. *Phys. Rev. Res.* **5**, 043141 (2023).
- Hafez, H. A. et al. Extremely efficient terahertz high-harmonic generation in graphene by hot Dirac fermions. *Nature* **561**, 507–511 (2018).
- Giorgianni, F. et al. Strong nonlinear terahertz response induced by dirac surface states in Bi₂Se₃ topological insulator. *Nat. Commun.* **7**, 11421 (2016).
- Uaman Svetikova, T. A. et al. Giant THz nonlinearity in topological and trivial HgTe-based heterostructures. *ACS Photonics* **10**, 3708–3714 (2023).
- Beck, M. et al. Impulsive terahertz radiation with high electric fields from an amplifier-driven large-area photoconductive antenna. *Opt. Express* **18**, 9251–9257 (2010).
- Helm, M. et al. The ELBE infrared and THz facility at Helmholtz-Zentrum Dresden-Rossendorf. *Eur. Phys. J.* **138**, 158 (2023).

24. Navaeipour, P. & Dignam, M. M. Effects of microscopic scattering on terahertz third harmonic generation in monolayer graphene. *Phys. Rev. B* **105**, 11431 (2022).
25. Seidl, A. et al. Pump-induced terahertz anisotropy in bilayer graphene. *Phys. Rev. B* **105**, 085404 (2022).
26. Mics, Z. et al. Thermodynamic picture of ultrafast charge transport in graphene. *Nat. Commun.* **6**, 7655 (2015).
27. König-Otto, J. C. et al. Slow noncollinear Coulomb scattering in the vicinity of the Dirac point in graphene. *Phys. Rev. Lett.* **117**, 087401 (2016).
28. Mikhailov, S. A. Non-linear electromagnetic response of graphene. *Europhys. Lett.* **79**, 27002 (2007).
29. Al-Naib, I., Poschmann, M. & Dignam, M. M. Optimizing third-harmonic generation at terahertz frequencies in graphene. *Phys. Rev. B* **91**, 205407 (2015).
30. Maleki, A. et al. Strategies to enhance THz harmonic generation combining multilayered, gated, and metamaterial-based architectures. *Light.: Sci. Appl.* **14**, 44 (2025).
31. Deinert, J.-C. et al. Grating-graphene metamaterial as a platform for terahertz nonlinear photonics. *ACS Nano* **15**, 1145–1154 (2021).
32. Tielrooij, K.-J. et al. Milliwatt terahertz harmonic generation from topological insulator metamaterials. *Light.: Sci. Appl.* **11**, 315 (2022).
33. Yang, Y. et al. Terahertz topological photonics for on-chip communication. *Nat. Photonics* **14**, 446–451 (2020).
34. Boyd, R. W., Gaeta, A. L. & Giese, E. Nonlinear optics. In *Springer Handbook of Atomic, Molecular, and Optical Physics*, 1097–1110 (Springer, 2008).
35. Alloatti, L. et al. 42.7 gbit/s electro-optic modulator in silicon technology. *Opt. Expr.* **19**, 11841–11851 (2011).
36. Chen, H.-T. et al. Active terahertz metamaterial devices. *Nature* **444**, 597–600 (2006).
37. Lee, Y.-S. *Principles of terahertz science and technology*, vol. 170 (Springer Science & Business Media, 2009).
38. Brown, E., McIntosh, K., Nichols, K. & Dennis, C. Photomixing up to 3.8 thz in low-temperature-grown gaas. *Appl. Phys. Lett.* **66**, 285–287 (1995).
39. Deumer, M. et al. Advancing terahertz photomixers through the integration of photoconductive antennas with optical waveguides. *APL Photonics* **10** (2025).
40. Yang, Y., Zhang, X., Hu, Z. & Wu, Y. Organic nonlinear optical crystals for highly efficient terahertz-wave generation. *Crystals* **13**, 144 (2023).
41. Su, Y. et al. Probing interface of perovskite oxide using surface-specific terahertz spectroscopy. *Ultrafast Sci.* **3**, 0042 (2023).
42. Khalatpour, A., Paulsen, A. K., Deimert, C., Wasilewski, Z. R. & Hu, Q. High-power portable terahertz laser systems. *Nat. Photonics* **15**, 16–20 (2021).
43. Dziom, V. et al. Observation of the universal magnetoelectric effect in a 3D topological insulator. *Nat. Commun.* **8**, 15197 (2017).
44. Kovalev, S. et al. Electrical tunability of terahertz nonlinearity in graphene. *Sci. Adv.* **7**, eabf9809 (2021).
45. Bovkun, L. et al. Topological phase diagram of mercury cadmium telluride quantum wells. *Phys. Rev. Mater.* **9**, 054602 (2025).
46. Brüne, C. et al. Quantum Hall effect from the topological surface states of strained bulk HgTe. *Phys. Rev. Lett.* **106**, 126803 (2011).
47. König, M. et al. Quantum spin Hall insulator state in HgTe quantum wells. *Science* **318**, 766–770 (2007).
48. Novik, E. G. et al. Band structure of semimagnetic $\text{Hg}_{1-y}\text{Mn}_y\text{Te}$ quantum wells. *Phys. Rev. B* **72**, 035321 (2005).
49. Burt, M. G. Fundamentals of envelope function theory for electronic states and photonic modes in nanostructures. *J. Phys.: Condens. Matter* **11**, 53 (1999).
50. Bir, G. & Pikus, G. *Symmetry and Strain-induced Effects in Semiconductors*. A Halsted Press book (Wiley, 1974).
51. Kuznetsov, K. A. et al. Topological insulator films for terahertz photonics. *Nanomaterials* **12**, 3779 (2022).
52. Cheng, B. et al. Efficient terahertz harmonic generation with coherent acceleration of electrons in the Dirac semimetal Cd_3As_2 . *Phys. Rev. Lett.* **124**, 117402 (2020).
53. Kovalev, S. et al. Non-perturbative terahertz high-harmonic generation in the three-dimensional Dirac semimetal Cd_3As_2 . *Nat. Commun.* **11**, 2451 (2020).

Acknowledgements

T.A.U.S., L.W.M., T.K. and G.V.A. acknowledge financial support from the Würzburg-Dresden Cluster of Excellence on Complexity and Topology in Quantum Matter ct.qmat (EXC 2147, DFG project ID 390858490). Parts of this research were carried out at ELBE at the Helmholtz-Zentrum Dresden - Rossendorf e. V., a member of the Helmholtz Association.

Author contributions

T.A.U.S., I. I., A.P., T.V.A.G.O., C.B., J.-C. D., G.L.P., A.A., A.P., T.K. and S.K. performed experiments. T.A.U.S. analyzed experimental data. T.A.U.S., A.P., T.K., S.W., M.H. and G.V.A. interpreted the experimental data. L.F., F.B., H.B., T.K. and L.W.M. provided HgTe samples. E.G.N. performed band structure calculations. T.A.U.S. and G.V.A. wrote the manuscript with input from all coauthors. G.V.A. supervised the project.

Funding

Open Access funding enabled and organized by Projekt DEAL.

Competing interests

The authors declare no competing interests.

Additional information

Supplementary information The online version contains supplementary material available at <https://doi.org/10.1038/s42005-025-02273-0>.

Correspondence and requests for materials should be addressed to Tatiana A. Uaman Svetikova or Georgy V. Astakhov.

Peer review information : *Communications Physics* thanks Kemeng Wang and the other, anonymous, reviewer(s) for their contribution to the peer review of this work. [A peer review file is available].

Reprints and permissions information is available at <http://www.nature.com/reprints>

Publisher's note Springer Nature remains neutral with regard to jurisdictional claims in published maps and institutional affiliations.

Open Access This article is licensed under a Creative Commons Attribution 4.0 International License, which permits use, sharing, adaptation, distribution and reproduction in any medium or format, as long as you give appropriate credit to the original author(s) and the source, provide a link to the Creative Commons licence, and indicate if changes were made. The images or other third party material in this article are included in the article's Creative Commons licence, unless indicated otherwise in a credit line to the material. If material is not included in the article's Creative Commons licence and your intended use is not permitted by statutory regulation or exceeds the permitted use, you will need to obtain permission directly from the copyright holder. To view a copy of this licence, visit <http://creativecommons.org/licenses/by/4.0/>.

© The Author(s) 2025